Journal of Scientific Computing manuscript No.
(will be inserted by the editor)

On Reconstruction from Non-uniform Spectral Data

Adityavikram Viswanathan · Anne Gelb · Douglas Cochran · Rosemary Renaut

Received: date / Accepted: date

In memory of David Gottlieb, beloved teacher, scholar, and friend. His pioneering work in spectral methods and in particular in resolving the Gibbs phenomenon has had a profound influence on this research.

Abstract This paper addresses the reconstruction of compactly supported functions from non-uniform samples of their Fourier transform. We briefly investigate the consequences of acquiring non-uniform spectral data. We summarize two often applied reconstruction methods, convolutional gridding and uniform re-sampling, and investigate the reconstruction accuracy as it relates to sampling density. Finally, we provide preliminary results from employing spectral re-projection methods in the reconstruction.

Keywords non-harmonic Fourier reconstruction · sampling density · convolutional gridding · spectral re-projection

1 Introduction

Let $f \in L^2(\mathbb{R})$ be compactly supported in $[-\pi, \pi]$. The approximation of f from the Fourier series coefficients, $\hat{f}(k) := \frac{1}{2\pi}\int_{-\pi}^{\pi} f(x)e^{-ikx}dx$, $k \in \mathbb{Z}$ is an often studied problem, [8, 25]. The approximation of f from non-uniform Fourier data $\hat{f}(\omega_k) := \frac{1}{2\pi}\int_{-\pi}^{\pi} f(x)e^{-i\omega_k x}dx$, ω_k not necessarily integers, has received relatively less attention, however. The two-dimensional version of this problem is most commonly encoun-

A. Viswanathan · D. Cochran
School of Electrical, Computer and Energy Engineering, Arizona State University, Tempe, AZ 85287-5706, USA
E-mail: {aditya.v,cochran}@asu.edu

A. Gelb · R. Renaut
School of Mathematical and Statistical Sciences, Arizona State University, Tempe, AZ 85287-1804, USA
E-mail: ag@math.la.asu.edu,renaut@asu.edu

tered in magnetic resonance imaging (MRI), where there are compelling arguments to acquire "k-space" (Fourier domain) samples along non-Cartesian trajectories [1]. We are particularly interested in the scenario where the Fourier samples are acquired with non-uniform density; for example, in MR applications, it is not uncommon to encounter sampling schemes with an abundance of samples at the low modes and sparse samples at the high modes. This variable density of coefficients makes the reconstruction process particularly challenging. Additionally, most real-world functions of interest are piecewise-analytic in nature. Fourier reconstruction of such functions suffer from the Gibbs phenomenon, [13], with non-uniform convergence at a local level and reduced order of convergence globally. In the Fourier domain, piecewise-analyticity manifests as a reduced (first order) decay rate of coefficients. The combination of slowly decaying Fourier coefficients and sparse measurements at high modes makes the reconstruction of piecewise-analytic functions from non-harmonic Fourier data especially challenging.

In this paper, we illustrate the problems posed by acquiring non-uniform[1] spectral data. We compare the kernel described by the non-uniform sampling pattern with the Dirichlet kernel and show that the non-uniform kernel has undesirable reconstruction properties. We then briefly summarize convolutional gridding, which is the most common reconstruction algorithm used in MR imaging for non-Cartesian sampling. We also discuss the uniform resampling method which, due to cost, is not as popular. The objective here is not to describe these methods in detail or compare them to other methods; rather, our motivation will be to study them with the intention of deducing relations between reconstruction error and sampling density. It turns out that the underlying problem is the poor recovery of high-frequency information, aggravated by the piecewise-smooth nature of the function. Consequently, we suggest the use of spectral re-projection schemes in the reconstruction process. Spectral re-projection involves reconstructing the function in an alternate, fast converging basis. The spectral re-projection process ensures that the high frequency modes in the Fourier basis (which have significant error) have exponentially small contributions in the reconstruction basis. It has been shown to be very effective in recovering piecewise-smooth functions from their uniform Fourier coefficients, [14], and has also been successfully applied to MR post-processing, [2, 3]. Our simulations show that these schemes provide comparable results to standard Fourier-based reconstruction methods while using far fewer coefficients. The ability to reconstruct functions without the high-mode coefficients makes for a significant reduction in scan acquisition time in an application such as MRI, leading to greater patient comfort, reduction of motion artifacts, and smaller turnaround times.

The rest of this paper is organized as follows: We begin by describing the difference between harmonic and non-harmonic Fourier reconstruction in Sec 2. In particular, we show that a "non-harmonic" Fourier partial sum does not converge to the underlying function, with illustrative examples for different sampling schemes. In Sec. 3, we summarize the frequently used convolutional gridding reconstruction method, and study the reconstruction error as a function of sampling density. Sec. 4 briefly summarizes the uniform re-sampling algorithm, which is an alternative reconstruction procedure for non-uniformly sampled spectral data. Use of a spectral re-projection scheme in the reconstruction with Gegenbauer polynomials is described in Sec. 5. We provide some

[1] The terms non-uniform and non-harmonic will be used interchangeably throughout this paper.

concluding remarks and future directions in Sec. 6.

The following sampling schemes will be referred to in the course of the paper:

1. Log Sampling: Samples in Fourier space are acquired at logarithmic intervals, with more samples acquired in lower frequencies. If ω_k are the nodes at which measurements are acquired, $|\omega_k|$ is logarithmically distributed between 10^{-v} and N, with $v > 0$ and $2N + 1$ being the total number of samples. Motivation for this sampling scheme can be found in MRI, where typical data acquisition schemes oversample the low frequencies of k-space while undersampling the high frequencies. Fig. 1(b) illustrates the log sampling scheme.
2. Jittered Sampling:

$$\omega_k = k \pm \tau_k, \quad \tau_k \sim U[0, \theta],\ k = -N, -(N-1), ..., N \tag{1}$$

Here $U[a, b]$ denotes a uniform distribution on the interval $[a, b]$. The τ_k's are independent, identically distributed (iid) random variables, and represent a uniform jitter about the equispaced nodes with a maximal jitter of θ. Further, both positive and negative jitters are equiprobable, with the sign of jitter at each node being independent of the sign of jitter at any other node. Fig. 1(a) illustrates the jittered sampling scheme.

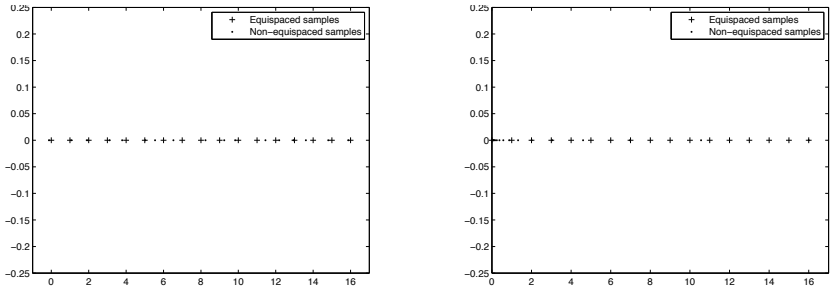

(a) Jittered sampling, $N = 16, \theta = 0.5$ (b) Log sampling, $N = 16, v = 1.5$

Fig. 1 Sampling schemes shown in the right half plane

2 Reconstruction from non-harmonic Fourier data

The Fourier partial sum

$$S_N f(x) = \sum_{|k| \le N} \hat{f}(k) e^{ikx} \tag{2}$$

constitutes the most popular method of approximating a function from its harmonic Fourier coefficients

$$\hat{f}(k) := \frac{1}{2\pi} \int_{-\pi}^{\pi} f(x) e^{-ikx} dx,\ k \in \mathbb{Z} \tag{3}$$

It is a simple exercise to show that $S_N f$ may be written as

$$S_N f(x) = (f * D_N)(x), \quad D_N(\eta) = \sum_{|k|\leq N} e^{ik\eta} \tag{4}$$

where $D_N(\eta)$ is the Dirichlet kernel, which is the Fourier partial sum approximation of the Dirac delta measure. Hence, for smooth and periodic f, the error component is purely due to truncation, with $S_N f \to f$ as $N \to \infty$. Moreover, the approximation exhibits spectral convergence. However, the same does not hold when we are given non-harmonic spectral data $\hat{f}(\omega_k)$. Consider reconstruction using the "non-harmonic" partial sum

$$P_N f(x) = \sum_{|k|\leq N} \hat{f}(\omega_k) e^{i\omega_k x}, \quad \hat{f}(\omega_k) := \frac{1}{2\pi} \int_{-\pi}^{\pi} f(x) e^{-i\omega_k x} dx \tag{5}$$

with ω_k not necessarily integers. In this case, we have

$$\begin{aligned} P_N f(x) &= \sum_{|k|\leq N} \hat{f}(\omega_k) e^{i\omega_k x} \\ &= \sum_{|k|\leq N} \left(\frac{1}{2\pi} \int_{-\pi}^{\pi} f(\eta) e^{-i\omega_k \eta} d\eta \right) e^{i\omega_k x} \\ &= \frac{1}{2\pi} \int_{-\pi}^{\pi} f(\eta) \sum_{|k|\leq N} e^{i\omega_k (x-\eta)} d\eta \\ P_N f(x) &= (f * A_N)(x), \quad A_N(\eta) = \sum_{|k|\leq N} e^{i\omega_k \eta} \end{aligned} \tag{6}$$

Fig. 2 demonstrates the behavior of the non-harmonic kernel $A_N(\eta)$ for both the jittered and logarithmic sampling distributions using various N. In either case, we note significant deviation from the Dirichlet kernel, with $A_N(\eta) \nrightarrow D_N(\eta)$ as N increases. This holds for any sampling distribution deviating from equispaced nodes, with the consequence being non-convergence of $P_N f$ to the true function, i.e.,

$$(f * A_N)(x) \nrightarrow f(x) \text{ as } N \text{ increases} \tag{7}$$

The kernel for log sampling is, in particular, not conducive for good reconstructions because of the large "mainlobe" and strong "sidelobes". Consequently, $P_N f(x) = (f * A_N)(x)$ is not localized – the reconstruction at any given point x_a has contributions from several points far away from and unrelated to x_a. This can be particularly troublesome in piecewise-smooth functions where Gibbs-like and other spurious artifacts[2] are seen. Representative reconstructions using either sampling scheme are shown in Fig. 3. Figs. 3(a) and 3(b) illustrate reconstruction of

$$f_1(x) = \cos(6x) \tag{8}$$

[2] These other spurious artifacts are caused by the convolution with $A_N(\eta)$ in Eqn. 6 and are unrelated to other types of noise inherent in any collection process of $\hat{f}(\omega_k)$.

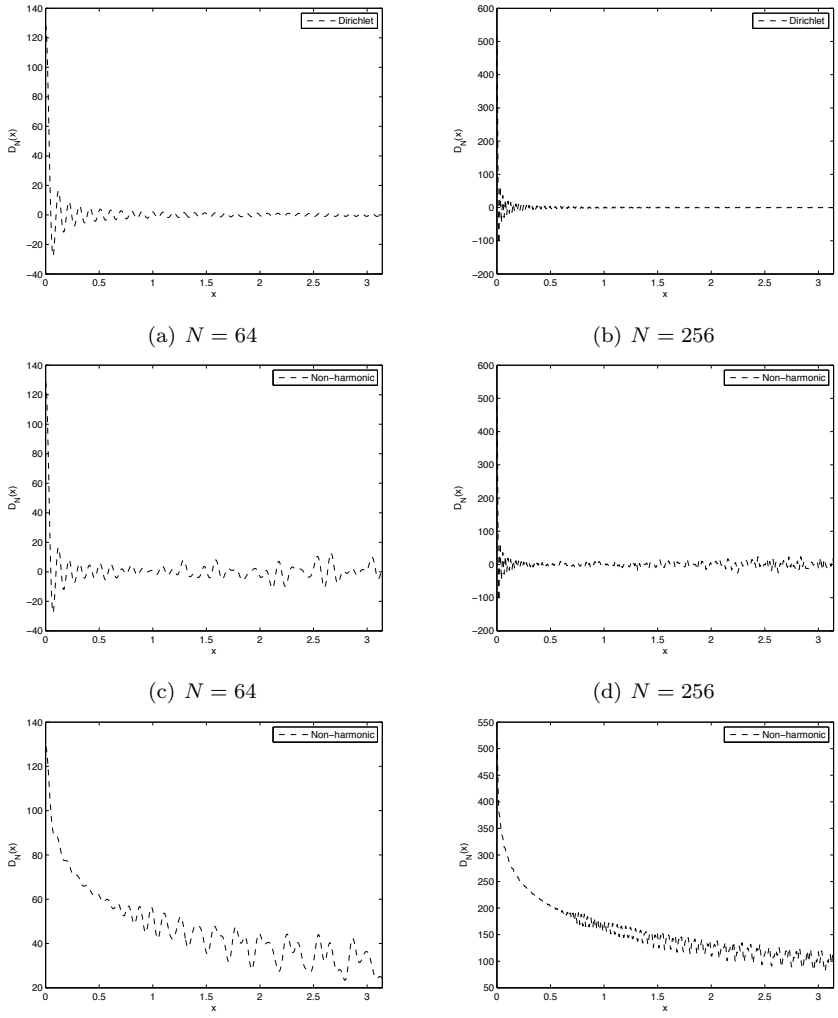

(a) $N = 64$ (b) $N = 256$

(c) $N = 64$ (d) $N = 256$

(e) $N = 64$ (f) $N = 256$

Fig. 2 Comparison of the Dirichlet kernel ((a) and (b)) and the non-harmonic kernel using jittered sampling ((c) and (d)) and log sampling ((e) and (f)) in the right half plane

using the jittered and log sampling schemes respectively, while Figs. 3(c) and 3(d) illustrate reconstruction of

$$f_2(x) = \begin{cases} \frac{3}{2} & -\frac{3\pi}{4} \le x < -\frac{\pi}{2} \\ \frac{7}{4} - \frac{x}{2} + \sin(x - \frac{1}{4}) & -\frac{\pi}{4} \le x < \frac{\pi}{8} \\ \frac{11}{4}x - 5 & \frac{3\pi}{8} \le x < -\frac{3\pi}{4} \\ 0 & \text{else} \end{cases} \tag{9}$$

These figures show that all functions (smooth or otherwise) are afflicted by reconstruction artifacts when starting with non-uniform spectral data. Moreover, as evidenced by Fig. 4, the artifacts are not a result of poor resolution. Fig. 4(a) plots $\|f - P_N f\|_2$ while

Fig. 4(b) plots $\|f - P_N f\|_\infty$ for the jittered sampling scheme and the piecewise-smooth test function. Both plots indicate no dependence of the error on N. In either case, the underlying cause is the poor reconstruction qualities of the kernel (Eqn. 7) described by the non-uniform modes.

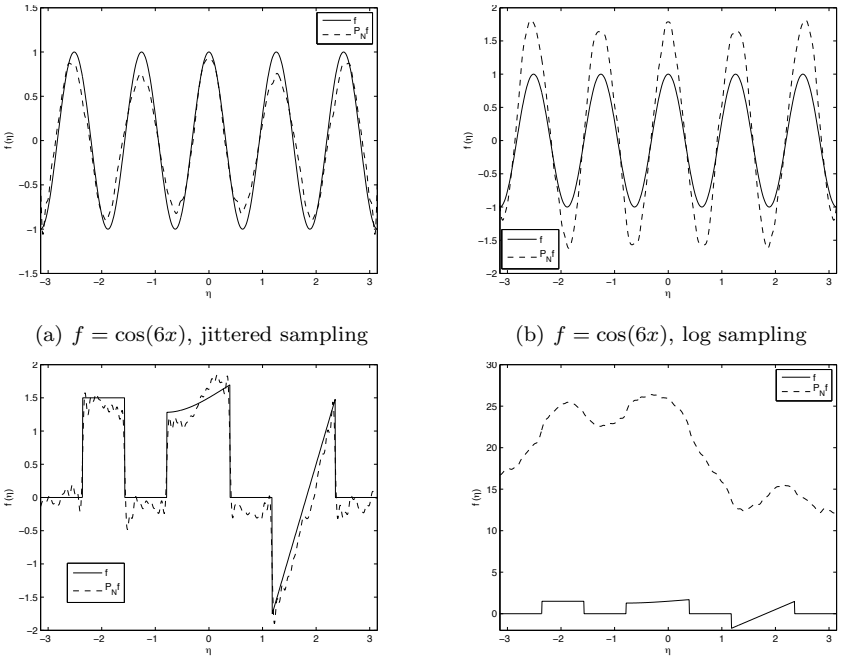

(a) $f = \cos(6x)$, jittered sampling

(b) $f = \cos(6x)$, log sampling

(c) Test function $f_2(x)$ (Eqn. 9), jittered sampling

(d) Test function $f_2(x)$ (Eqn. 9), log sampling

Fig. 3 Reconstruction using the non-harmonic partial sum, $N = 64$

3 Reconstruction using convolutional gridding

Besides identifying the reasons for the poor reconstruction quality, Sec. 2 demonstrates a reconstruction method which fails for non-uniform spectral data. It is illustrative to think of the reconstruction procedure as an approximation of the inverse Fourier integral $\int_{-\infty}^{\infty} \hat{f}(\omega) e^{i\omega x} d\omega$. Clearly, with non-uniform data, we cannot use the uniform trapezoidal quadrature rule which the non-harmonic partial sum describes. However, we can try to "fix" this by employing a partial sum of the form

$$S_N \tilde{f}(x) := \sum_{k=-N}^{N} \alpha_k \hat{f}(\omega_k) e^{i\omega_k x} \tag{10}$$

where the α_k correspond to weights of a non-uniform trapezoidal quadrature rule and are known in the MR imaging community as density compensation factors (DCFs).

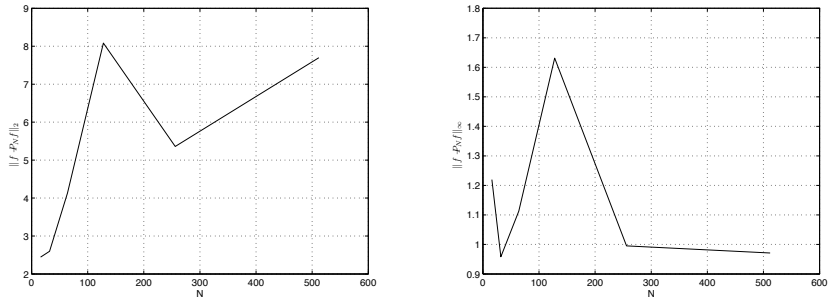

(a) $\|f - P_N f\|_2$ (b) $\|f - P_N f\|_\infty$

Fig. 4 Reconstruction error $\|f - P_N f\|$, for test function $f_2(x)$ (Eqn. 9) as a function of N using jittered sampling

One simple scheme for generating DCFs is as follows:

$$\alpha_k = \omega_{k+1} - \omega_k \tag{11}$$

It is easy to see that for the log sampling scheme, α_k would take small values at the low modes and large values at the high modes. In two-dimensions, we may compute a Voronoi tessellation of the non-Cartesian nodes and then assign individual cell areas as the density compensation weights. Several other methods of density compensation exist and generation of optimal DCFs is a research problem in itself. The interested reader is referred to [16, 20] for two such methods popular in the MR imaging community.

The importance of density compensation is reinforced by the plots in Fig. 5. The wide disparity in the values of the DCFs required to satisfy the quadrature rule for log sampling is shown in Fig. 5(a). Figs. 5(b) and (c) display the reconstruction plots without and with use of density compensation respectively. The log sampling scheme was used to generate the Fourier samples and the DCFs in Eqn. 11 were employed.

While the density compensated sum in Eqn. 10 performs a better job at reconstructing the function, the computational cost associated with its evaluation is significant. Unlike the standard Fourier partial sum, the fast Fourier transform (FFT) cannot be applied to speedup the $\mathcal{O}(N^2)$ evaluations since the FFT requires equispaced input data and equispaced output evaluation nodes. This can be a significant problem in multiple dimensions. Hence, a speedup mechanism was devised to compute non-uniform sums such as Eqn. 10 efficiently. While this procedure goes by several names – the non-uniform FFT, [9], the non-equispaced FFT, [10], or FFTs for non-uniform grids, [24] – it is commonly known as convolutional gridding, [16,19], in the MR imaging community. A summary of the convolutional gridding procedure is provided below.

One would imagine that any attempt at computational speedup would incorporate the FFT algorithm. Therefore, the convolutional gridding procedure involves moving from the non-uniform measurements to an equispaced grid (gridding), with the mapping achieved via a convolution operation. Note that we have to use the non-uniform trapezoidal quadrature rule (or density compensation) to approximate the convolution as a sum. Let ϕ be a smooth function whose properties will be enumerated a little later. The Fourier transform $\hat{f}$ of a compactly supported function is continuous. Hence, $\hat{f} * \hat{\phi}$ is a continuous function. We choose to evaluate $\hat{f} * \hat{\phi}$ at equispaced grid points so as to be amenable to an FFT evaluation. Partial Fourier or filtered Fourier reconstruction

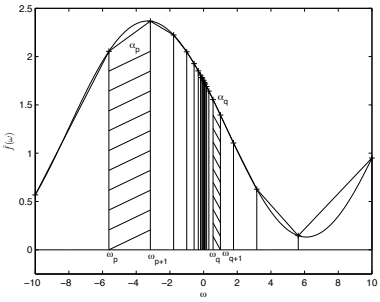

(a) Non-uniform trapezoidal quadrature

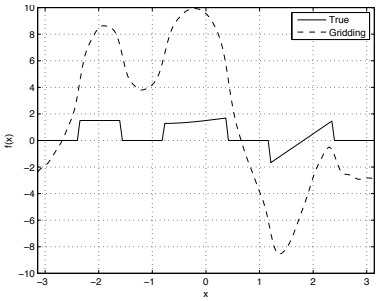

(b) Reconstruction without density compensation, $N = 32$

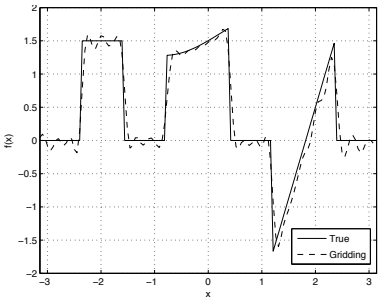

(c) Reconstruction with density compensation, $N = 32$

Fig. 5 Density compensation

(evaluated using the FFT) yields the corresponding physical-space function $f \cdot \phi$, from which we may divide out ϕ (an operation known as compensation or de-apodization) to obtain our approximation to f. The steps of the convolutional gridding algorithm are enumerated in Algorithm 1 while a graphical illustration of the FFT reconstruction and window compensation is provided in Fig. 6.

3.1 The window function ϕ

Since our goal is to reduce computational cost, we would like that the gridding process (finite sum approximation of the convolution) be relatively inexpensive to compute. This requires that the number of terms in the convolution sum be small; since $\hat{f}$ has infinite support, we would prefer $\hat{\phi}$ to have compact support.

However, this would imply that the physical space function ϕ is of infinite extent. Since we reconstruct periodic repetitions of f, there is the distinct possibility of aliasing artifacts appearing, i.e., reconstruction values from other periods showing up in the principal domain of reconstruction $[-\pi, \pi)$. This is especially problematic if the number of Fourier measurements acquired is small or only just sufficient to resolve the function. Therefore, we want ϕ to be supported in $[-\pi, \pi]$. Further, we require the window function to be non-zero in this interval since we divide out ϕ to obtain f.

These are contradictory requirements since a function cannot be bandlimited in both domains. Practical window functions therefore attempt to be *essentially bandlimited*; i.e.,

$$\begin{aligned} &\hat{\phi}(\omega) \approx 0 \ |\omega| > q, \ q \in \mathbb{R}, \text{small} \\ &\phi(x) \approx 0 \ |x| > \pi \\ &\phi(x) \neq 0 \ x \in [-\pi, \pi] \end{aligned} \tag{12}$$

Popular window functions include the Gaussian and Kaiser Bessel functions[3]. Observe that the window function is independent of filtering, which is always applied since the underlying functions are generally piecewise-smooth and can contain noise.

Algorithm 1 The convolutional gridding algorithm

Given: $\hat{f}$ at the non-equispaced measurement nodes ω_k
Choose: Truncation parameter q
Interpolating function ϕ

1. Interpolation to equispaced nodes:
$\hat{\tilde{g}}(k) = \sum_{m \text{ st. } |k-\omega_m| \leq q} \alpha_m \hat{f}(\omega_m) \hat{\phi}(k - \omega_m), \quad k = -N, ..., N$
2. Standard FFT computation:
$S_N \tilde{g}(x_p) = \sum_{k=-N}^{N} \hat{\tilde{g}}(k) e^{ikx_p}, \quad x_p = -\pi + \frac{2\pi p}{N}, \quad p = 0, ..., N-1$
3. Compensation for use of the interpolating function:
$S_N \tilde{f}(x_p) = \frac{\tilde{g}(x_p)}{\phi(x_p)}$

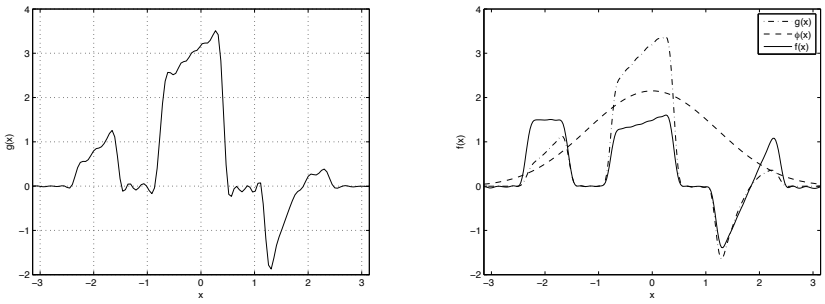

(a) FFT reconstruction (b) Compensation

Fig. 6 Illustration of convolutional gridding, $N = 128$

[3] We note that it may be useful to define $\phi(x)$ as a mollifier with properties such as those described in [26, 27], and will be studied in future investigations.

To demonstrate the effectiveness of convolutional gridding, we introduce the test function

$$f_3(x) = \begin{cases} \sin(3x) & x < 0 \\ e^{-2x} & x \geq 0 \end{cases} \tag{13}$$

Fig. 7(a) shows the result of gridding reconstruction of the test function in Eqn. 13. Fig. 7(b) shows the reconstruction of a cross-section of a brain scan obtained from the McGill BrainWeb database, [6,7,17,18,21]. This was a T1 scan of a normal brain with 1mm slice thickness and no noise or RF field non-uniformities. In both cases, spectral data was acquired using the log sampling scheme and the results were further processed using a fourth-order exponential filter.

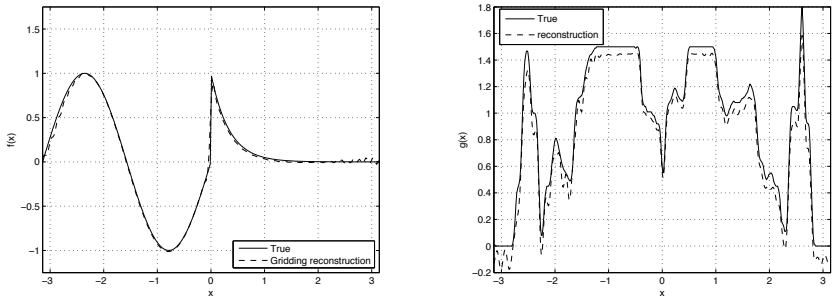

(a) Reconstruction of test function $f_3(x)$ (Eqn. 13), $N = 128$, jittered sampling

(b) Reconstruction of a brain cross-section from log spectral samples

Fig. 7 Reconstruction using convolutional gridding, processed using a fourth-order exponential filter

3.2 Error in convolutional gridding reconstruction

We now derive error bounds for the gridding process and the resulting reconstruction, which requires the following definition.

Definition 1 *(Minimum sampling density d_k)* Let the *q-vicinity* of k ($q > 0$) be the set $\{\mathcal{P} = \omega \text{ st. } |k - \omega| \leq q,\ k \in \mathbb{Z},\ \omega, q \in \mathbb{R}\}$. The *q-vicinity* refers to the region around any equispaced coefficient. Let Δ_k be the maximum distance between sampling points in the q-vicinity of k; i.e., $\Delta_k = \max_{p \in \mathcal{P}} |\omega_{p+1} - \omega_p|$. In this q-vicinity, we define the *minimum sample "density"* d_k to be the number of sample points per unit interval; i.e., $d_k = \frac{1}{\Delta_k}$.

Theorem 1 (Convolutional gridding error) *Let ω_k denote the non-uniformly sampled modes and $\hat{f}(\omega_k)$ the Fourier transform measurements at these modes. Let $\hat{\phi}$ denote the gridding window function and $\hat{g} = \hat{f} * \hat{\phi}$ denote the true gridding coefficients. Let $\tilde{\hat{g}}$ denote the approximate gridding coefficients obtained by using a finite sum and the DCFs in Eqn. 11. Let q be the window function truncation parameter; i.e., $\hat{\phi}(\omega) = 0$ for $|\omega| > q$. Let d_k be the minimum sample density in the q-vicinity of k. Then, the gridding error at mode k is bounded by $e(k) \leq C \cdot \frac{1}{d_k^3}$, $k = -N, ..., N$ for some positive constant C.*

Proof The error in each of the equispaced Fourier coefficients after gridding is given by

$$\hat{g}(k) - \hat{\tilde{g}}(k) = \int_{-\infty}^{\infty} \hat{f}(\omega)\hat{\phi}(k-\omega)d\omega - \sum_{p \text{ st. } |k-\omega_p|\leq q} \alpha_p \hat{f}(\omega_p)\hat{\phi}(k-\omega_p) \tag{14}$$

Let us evaluate the error in approximating the integral in the interval (ω_p, ω_{p+1}). Substituting Eqn. 11 for the density compensation factors α_p and using the trapezoidal quadrature rule, we have

$$e_p = \int_{\omega_p}^{\omega_{p+1}} \hat{f}(\omega)\hat{\phi}(k-\omega)d\omega - \frac{|\omega_{p+1}-\omega_p|}{2}\left(\hat{f}(\omega_p)\hat{\phi}(k-\omega_p) + \hat{f}(\omega_{p+1})\hat{\phi}(k-\omega_{p+1})\right)$$

The trapezoidal quadrature rule, [4], yields

$$e_p \leq \frac{|\omega_{p+1}-\omega_p|^3 v_p}{12} \tag{15}$$

where

$$\begin{aligned} v_p &= \left.\frac{d^2\left(\hat{f}(\omega)\hat{\phi}(k-\omega)\right)}{d\omega^2}\right|_{\omega=\zeta}, \quad \zeta \in [\omega_p, \omega_{p+1}] \\ &= \left.\hat{f}(\omega)\hat{\phi}^{(2)}(k-\omega)\right|_{\omega=\zeta} - 2\left.\hat{f}^{(1)}(\omega)\hat{\phi}^{(1)}(k-\omega)\right|_{\omega=\zeta} + \left.\hat{f}^{(2)}(\omega)\hat{\phi}(k-\omega)\right|_{\omega=\zeta} \end{aligned}$$

We note that $\hat{f}, \hat{\phi}$ and their derivatives are finite in the interval (ω_p, ω_{p+1}); hence v_p is bounded. The total error is the error over all intervals of integration; i.e., $e(k) = \sum_p e_p$. However, the window function is non-zero only over the q-vicinity of k. Hence,

$$\begin{aligned} \hat{g}(k) - \hat{\tilde{g}}(k) &\lesssim \sum_{p \text{ st. } |k-\omega_p|\leq q} e_p \\ \left|\hat{g}(k) - \hat{\tilde{g}}(k)\right| &\leq \sum_{p \text{ st. } |k-\omega_p|\leq q} \frac{|\omega_{p+1}-\omega_p|^3 \ |v_p|}{12} \\ &\leq \kappa \sum_{p \text{ st. } |k-\omega_p|\leq q} |\omega_{p+1}-\omega_p|^3, \quad \kappa = \max_p \frac{|v_p|}{12} \\ &\leq C \cdot \Delta_k^3, \quad \text{for some positive constant } C \\ &= C \cdot \frac{1}{d_k^3} \quad \text{using Def. 1} \quad \square \end{aligned}$$

Errors in the gridding procedure using the test function $f_3(x)$ in Eqn. 13 for the jittered sampling and log sampling schemes are plotted in Figs. 8(a) and (b) respectively along with the error bounds derived in Theorem 1. The "true" coefficients were computed by approximating the convolution using an equispaced sum on a fine grid (> 2000 points). The constant C was chosen such that $C > \max_k \ d_k^3 \left|\hat{g}(k) - \hat{\tilde{g}}(k)\right|$. We used a Gaussian window function with truncation parameter $q = 12$ to satisfy Eqn. 12.

The error for jittered sampling is somewhat random, as one would expect from the sampling pattern. Some of the low frequency coefficients have more error than some

of the high frequency coefficients and vice-versa. The error pattern for log sampling is more interesting. As dictated by the sample density, the high mode coefficients show significant error in comparison to the low modes. This makes reconstructing functions with variation (significant high-mode content) or piecewise-smooth functions (slowly decaying coefficients) challenging.

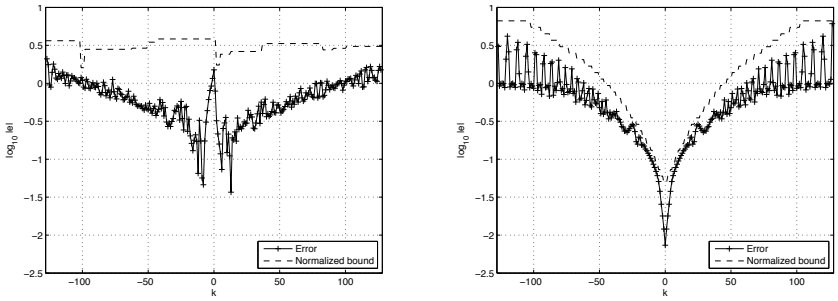

(a) Jittered sampling (b) Log sampling

Fig. 8 Gridding error and the associated error bound

We now turn our attention to the physical-space reconstruction error. If we assume that the compensation step of the reconstruction (where we divide out the window function) can be performed without error, the physical-space reconstruction error is purely due to partial Fourier approximation using the gridding coefficients. We have

$$\begin{aligned} e(x) \approx g(x) - S_N\tilde{g}(x) &= g(x) - S_N g(x) + S_N g(x) - S_N\tilde{g}(x) \\ &= \sum_{|k|>N} \hat{g}(k)e^{ikx} + \sum_{|k|\leq N} \left(\hat{g}(k) - \hat{\tilde{g}}(k)\right) e^{ikx} \end{aligned} \tag{16}$$

The first component is the standard Fourier truncation error. This has been well studied and we provide the error bounds from [15]. For $f \in C^s[-\pi,\pi], s > \frac{1}{2}$, we have

$$|g - S_N g| = \left| \sum_{|k|>N} \hat{g}(k)e^{ikx} \right| \leq \frac{C_1}{N^{s-1/2}} \|f^{(s)}\|_{L^2[-\pi,\pi]} \tag{17}$$

$$\|g - S_N g\|_2 \leq C_2\, N^{-s}\, \|f^{(s)}\|_{L^2[-\pi,\pi]} \tag{18}$$

where C_1, C_2 are positive constants independent of N. We are, however, interested in the error bounds for piecewise-smooth functions since our problem statement specifically deals with the reconstruction of compactly supported functions. If f is piecewise-smooth, then we know that $S_N g$ suffers from the Gibbs phenomenon. The maximum error occurs in the vicinity of a jump and is approximately 1.09 of the jump value. There is also a reduced order of convergence with $\|g - S_N g\|_2 = \mathcal{O}\left(N^{-1/2}\right)$.

The second term in Eqn. 16 is the error due to the non-uniform sampling acquisition and the gridding process. We have

$$\begin{aligned} |S_N g(x) - S_N \tilde{g}(x)| &= \left| \sum_{|k| \leq N} \left(\hat{g}(k) - \hat{\tilde{g}}(k) \right) e^{ikx} \right| \\ &\leq \sum_{|k| \leq N} \left| \hat{g}(k) - \hat{\tilde{g}}(k) \right| \\ &\leq C \sum_{|k| \leq N} \frac{1}{d_k^3} \end{aligned} \tag{19}$$

Let $H(\omega_k, N) := \sum_{|k| \leq N} \frac{1}{d_k^3}$. This term is plotted as a function of N for the log sampling pattern in Fig. 9. We observe that it increases rapidly with N, indicating that the error in the reconstruction would increase at a similar rate.

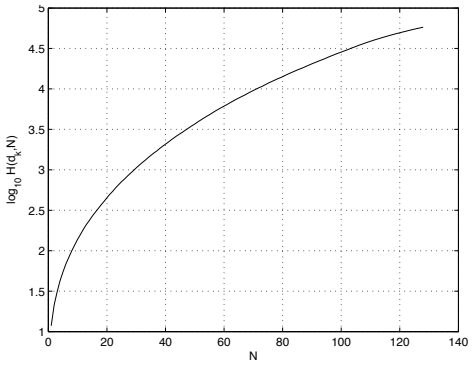

Fig. 9 Plot of $H(\omega_k, N)$ as a function of N for log sampling

It is interesting to note that the two error components in Eqn. 16 have differing characteristics; the gridding error (Eqn. 19) increases with N while the Fourier truncation error decreases with N. For sampling locations close to the integers, we expect that the rate of decrease of truncation error exceeds the rate of increase of gridding error. The net result is a decreased overall approximation error with increase in N. However, with sampling schemes such as log sampling, this does not hold – the error in gridding coefficients increases rapidly to the point where it is advantageous to use only a few of them in the reconstruction.

This observation is illustrated in Fig. 10 where a test function (Eqn. 20) is reconstructed from its log spectral samples. The figures show the reconstruction both before and after dividing out the window function of Eqn. 12 where again we have used a Gaussian window with truncation parameter $q = 12$. Figs. 10(a)-(c) plot the reconstruction using different numbers ($N = 20, 60, 128$) of the regridded coefficients while Fig. 10(d) plots the norm of the squared error in the pre-compensated reconstruction. The plots reveal that the reconstruction error initially decreases as we use more of the regridded coefficients; however, after about $N = 60$, performance deteriorates with the

reconstruction error increasing.

$$f_4(x) = \begin{cases} -1 & -2.5 \le x < -\frac{\pi}{4} \\ e^{-x} & 0 \le x < \frac{\pi}{4} \\ 1 + \frac{\cos(5x)}{2} & 1.25 \le x < 2.75 \\ 0 & \text{else} \end{cases} \tag{20}$$

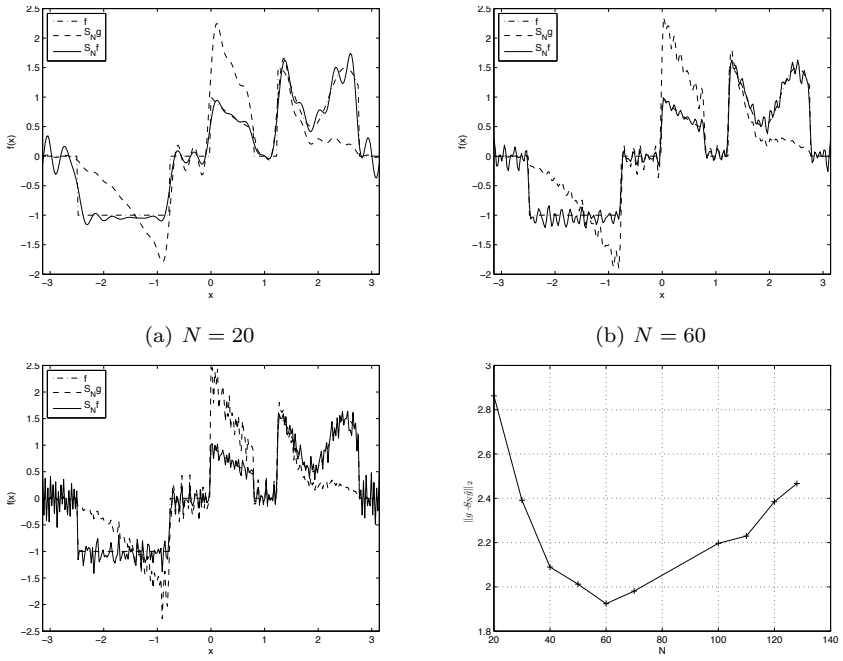

(a) $N = 20$ (b) $N = 60$

(c) $N = 128$ (d) $\|g - S_N \tilde{g}\|_2$

Fig. 10 Reconstruction of a test function from log spectral samples using convolutional gridding

It has been experimentally observed that the gridding algorithm works best when the sampling density varies significantly, as is the case with log sampling. Results using the gridding algorithm and jittered sampling, where the sampling density is, on average, uniform, are not optimal. In particular, other methods, such as the one described in Sec. 4 perform much better.

4 An Alternative Reconstruction Algorithm – Uniform Re-sampling

A more intuitive, albeit computationally intensive reconstruction procedure for non-uniform spectral data is the uniform re-sampling (URS) algorithm, [22,23]. This method seeks to obtain a least squares approximation to the equispaced coefficients given the non-uniform measurements. It is a two step reconstruction procedure

1. Recover Fourier coefficients at equispaced nodes
2. Reconstruct the function using a Fourier partial sum approximation

Note that the second step is amenable to applying the FFT and we may choose to use filtered approximations to accelerate convergence. The recovery of equispaced coefficients is achieved using the Shannon sampling theorem. In its more traditional form, this theorem is a physical space interpolation formula using sinc interpolants for functions with bandlimited spectral content. We face the dual scenario, requiring the recovery of Fourier data of a compactly supported function. Let $f \in L^2(-\pi, \pi)$. Shannon's sampling theorem then says that we can recover the Fourier transform of f at any point ω given the (infinite) Fourier samples at the integers; i.e.,

$$\hat{f}(\omega) = \sum_{k=-\infty}^{\infty} \hat{f}(k)\text{sinc}(\omega - k), \quad \omega \in \mathbb{R} \tag{21}$$

Of course we have to restrict ourselves to the finite dimensional case, and since we are given non-uniform measurements, we have to invert the above system of equations to recover the equispaced coefficients. Since this is essentially a convolution with shifted sinc interpolants, we may write the above relation as a linear system of equations. Let $y = \hat{f}(m)$, $m = -N, ..., N$, denote the equispaced Fourier coefficients we seek. If $b = \hat{f}(\omega_k)$, $k = 0, ..., M-1$, are the set of measurements and A is the matrix with elements $a_{ij} = \text{sinc}(\omega_i - j), i = 0, ..., M-1$, $j = -N, ..., N$, we may write

$$Ay = b \tag{22}$$

We compute a least-squares minimum norm solution $\tilde{y}$ of the form $\tilde{y} = A^+ b$, where A^+ is the Moore-Penrose pseudoinverse computed using the singular value decomposition (SVD). Depending on the sampling pattern, A can have a large condition number. In such cases, use of regularization in computing the solution is advisable. Results in this paper use the truncated SVD.

Reconstruction of test function $f_2(x)$ (Eqn. 9) using this method from its log spectral samples is illustrated in Figs. 11 and 12. Fig. 11(a) plots the high-mode recovered equispaced Fourier coefficients, while Fig. 11(b) plots the corresponding error in recovering these coefficients. The function reconstruction is shown in Fig. 12. The coefficient recovery error trend is similar to that seen with the convolutional gridding algorithm and confirms the dependence on the sampling trajectory. The same arguments made with regard to the number of "good" or accurate coefficients and their use in function reconstruction apply here too. Note that it is difficult to perform error analysis with this reconstruction scheme since we cannot construct pointwise error estimates for inverse problems. A further example is provided in Fig. 13 where $f_3(x)$ is reconstructed from its jittered samples. Here, we find that the reconstruction accuracy is much better than the previous example. The Gibbs artifact remains and filtering or other techniques are required to mitigate this problem, but the error due to non-uniform spectral sampling is small.

From the two examples, we see that the quality of reconstruction depends on the sampling pattern. This trend is also seen in the condition number of the sinc matrix. Jittered sampling results in a well conditioned matrix which can be inverted easily. Log sampling, however, results in a large condition number ($\mathcal{O}(10^{17})$), with the result being that the system of equations cannot be solved accurately. The artifacts seen in Fig. 11 are a direct consequence of this. The plot of singular values for the two sampling

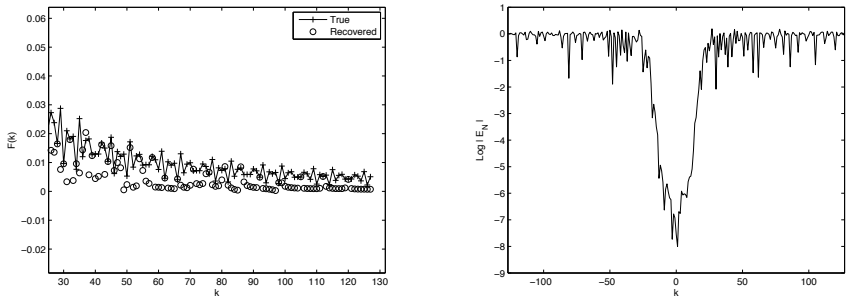

(a) Recovered high-mode equispaced Fourier coefficients (b) Error in the interpolated coefficients

Fig. 11 Reconstruction using URS, $N = 128$

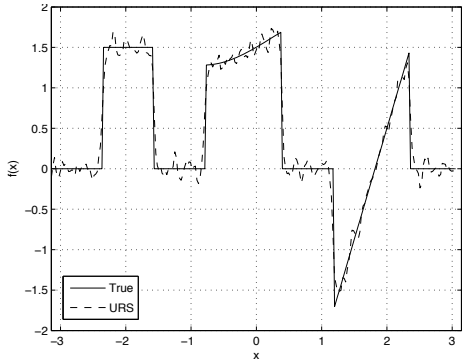

Fig. 12 Function reconstruction using URS, $N = 128$

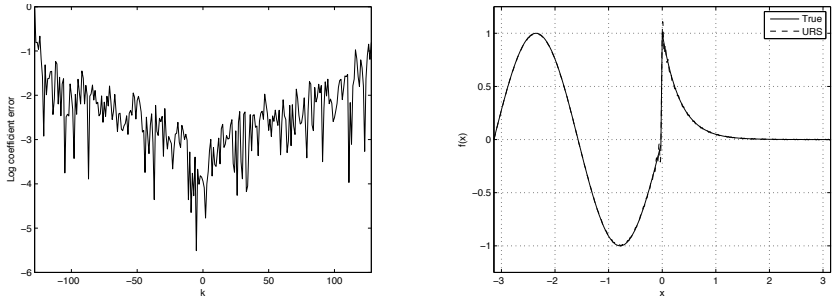

(a) Error in the interpolated coefficients (b) Function reconstruction

Fig. 13 Reconstruction of $f_3(x)$ using URS, $N = 128$

schemes are shown in Fig. 14 and can be seen to concur with the reconstruction results. Finally, Table 1 provides further numerical evidence that the condition number of the matrix depends on the sampling pattern. The condition number of the sinc matrix for jittered sampling is tabulated for different values of the jitter (parameter θ in Eqn.

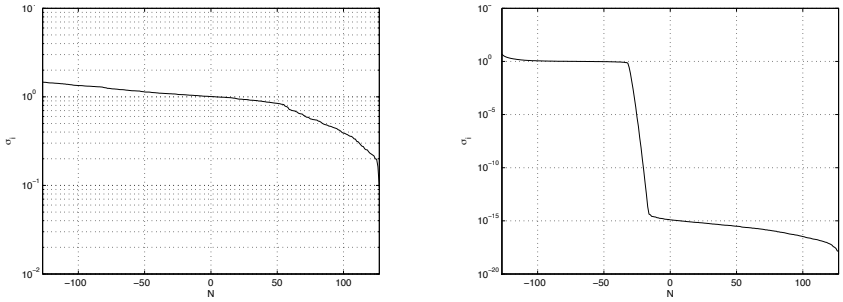

(a) Jittered sampling (b) Log sampling

Fig. 14 Plot of singular values of the sinc system matrix, $N = 128$

Maximal jitter, θ	0.1	0.5	1	5	10
Condition number	1.371	27.806	1.690×10^3	1.137×10^8	1.875×10^9

Table 1 Dependence of the sinc matrix condition number on the sampling pattern (Jittered sampling, $N = 128$)

1). It can be seen that as the jitter increases, i.e., the samples get more irregular, the condition number increases.

5 Spectral Re-projection

Piecewise-smooth functions, such as the brain scan cross-section in Fig. 7(b), are commonly encountered in real life. As we know, approximation of such functions from spectral data suffers from the Gibbs phenomenon. The main effects of the Gibbs phenomenon – non-uniform convergence at a local level and reduced order of convergence at a global level – are particularly troublesome in an application such as MR imaging. The non-uniform convergence leads to oscillations in the vicinity of discontinuities or smearing when subjected to filtering, which can cause loss of detail at tissue boundaries. Besides impacting the visual quality of the scan, such artifacts also reduce the accuracy of subsequent image processing tasks such as edge detection, segmentation or feature recognition. The interested reader is referred to [3] for an example of post-processing MR scans using spectral re-projection principles. The reduced order of convergence necessitates collection of a large number of spectral coefficients in the scanning procedure. This leads to an increase in scan time and can have other consequences such as patient discomfort or motion artifacts in the process of acquiring the scan.

A brief summary of spectral re-projection is in order before we see its application in the current problem. The reader is referred to classical works such as [14] for an in-depth perspective on the subject. Spectral data constitutes a global representation; a Fourier reconstruction at some point x ties together information about the function over the entire domain $(-\pi, \pi)$. We can see how this can be troublesome in discontinuous functions – the reconstruction on either side of a discontinuity uses information from the other side, leading to loss of localization and non-physical oscillations. Consequently, spectral re-projection schemes require reconstruction in each smooth interval. The edge detection required to identify intervals of smoothness is a research problem in itself.

We have found the concentration method of edge detection, [11, 12], and iterative formulations of the same (e.g., [28]), to be adequate in identifying the jump information.

Within an interval of smoothness, reconstruction is performed using an alternate, specifically chosen basis known as a *Gibbs complementary* basis. This basis is orthonormal, supports exponential reconstruction accuracy, and has the property that high modes of the Fourier basis have exponentially small projections on low modes of the reconstruction basis. Let $\{\psi_l\}$, $l = 0, 1, ...$ be such a basis. The m-term approximation of a function f using $\{\psi_l\}$ is given by

$$P_m f(x) = \sum_{l=0}^{m} c_l \psi_l(x), \quad c_l = \frac{\langle f, \psi_l \rangle_w}{\|\psi_l\|_w^2} \tag{23}$$

where w denotes a weight and $\langle \cdot, \cdot \rangle_w$ denotes a weighted inner product. The significance of the method lies in the observation that f can be replaced by its $(2N+1)$-term Fourier expansion f_N in the inner product in Eqn. 23 while still retaining exponential reconstruction accuracy. This is a profound statement which says that a poorly converging $(2N+1)$-term Fourier expansion contains sufficient information to recover and approximate the function with exponential accuracy. The consequent form of the inner product gives the method its name – Fourier spectral data is re-projected to Gibbs complementary basis coefficients.

In the context of reconstructing functions from non-uniform spectral data and sampling patterns such as log sampling, spectral re-projection has an added advantage. From Theorem 1, we see that the recovered equispaced coefficients at a particular mode have an error which depends on the sample density (or inter-sample spacing) in the vicinity of the mode. For variable sampling density schemes such as log sampling, this results in large errors in the high-mode coefficients as illustrated in Fig. 8. However, by design, the spectral re-projection of high-mode Fourier coefficients has exponentially low contributions on the low modes of the reconstruction basis. Hence, the error induced by the sampling scheme is exponentially damped by using spectral re-projection reconstructions. Further, the fast convergence properties of the Gibbs complementary basis means that we can start with a much smaller number of coefficients.

We can quantify these intuitive arguments by studying the the reconstruction error in the spectral re-projection reconstruction. Let us assume that the equispaced coefficients required for re-projection are obtained from convolutional gridding and that we use Gegenbauer polynomials $C_l^{\lambda}(x)$ for reconstruction[4]. We shall assume that smooth intervals in the function can be identified without error. The following is an outline of the steps involved in reconstruction:

1. Convolutional gridding to obtain coefficients on the equispaced grid ($\hat{\tilde{g}}$).
2. Re-projection of the $2N+1$-term Fourier expansion $S_N\tilde{g}$ to obtain Gegenbauer expansion coefficients ($\langle S_N\tilde{g}, C_l^{\lambda} \rangle$).
3. Function reconstruction using the Gegenbauer partial sum $P_m S_N \tilde{g}$

Further, we shall assume that the compensation step where we divide out the window function in Eqn. 12 can be performed without error; i.e., $\|f - P_m S_N \tilde{f}\| \approx \|g - P_m S_N \tilde{g}\|$. We then have

$$\|g - P_m S_N \tilde{g}\| \leq \|g - P_m g\| + \|P_m g - P_m S_N g\| + \|P_m S_N g - P_m S_N \tilde{g}\| \tag{24}$$

[4] See [14] for basic properties of $C_l^{\lambda}(x)$ and admissibility requirements for λ and m in Eqn. 23.

The first term is known as the *regularization error*. The classical result, [14], is that for $\lambda = \gamma m$, $\gamma > 0$, constant,

$$\|g - P_m g\|_\infty \leq A\zeta^m \tag{25}$$

where A is some positive constant and $\zeta = \dfrac{(1+2\gamma)^{1+2\gamma}}{2^{1+2\gamma}\rho\gamma^\gamma(1+\gamma)^{1+\gamma}}$. For $\rho \geq 1$, ζ can be shown to be less than one. The second term in Eqn. 24 is the *truncation error* and classical results (e.g., [14]) show that for $\lambda = \alpha N, m = \beta N$, α, β constants, this error can be bounded as

$$\|P_m g - P_m S_N g\|_\infty \leq A\zeta_T^N \tag{26}$$

where A grows at most as a fixed degree polynomial of N and $\zeta_T = \dfrac{(\beta+2\alpha)^{\beta+2\alpha}}{(2\pi)^\alpha \alpha^\alpha \beta^\beta}$. For carefully chosen λ, m ($\alpha = \beta \leq \frac{2\pi}{27}$), we have $\zeta_T < 1$. The third term in Eqn. 24 is due to gridding. For ease of analysis, we shall assume we are given a Fourier partial expansion in the interval $[-\pi, \pi]$. This result can be generalized to any other interval by suitable scaling.

$$\begin{aligned}
&\|P_m S_N g - P_m S_N \tilde{g}\|_\infty \leq \\
&\qquad \max_{-1\leq x\leq 1} \left| \sum_{l=0}^{m} \frac{C_l^\lambda(x)}{h_l^\lambda} \int_{-1}^{1} (1-\eta^2)^{\lambda-1/2} C_l^\lambda(\eta) \sum_{|k|\leq N} \left(\hat{g}(k) - \hat{\tilde{g}}(k)\right) e^{i\pi k\eta} d\eta \right| \\
&\qquad \leq \sum_{l=0}^{m} \sum_{|k|\leq N} \frac{C_l^\lambda(1)}{h_l^\lambda} \left| \int_{-1}^{1} (1-\eta^2)^{\lambda-1/2} C_l^\lambda(\eta) \left(\hat{g}(k) - \hat{\tilde{g}}(k)\right) e^{i\pi k\eta} d\eta \right| \\
&\qquad \leq C \sum_{l=0}^{m} \sum_{|k|\leq N} \frac{1}{d_k^3} \left| \frac{C_l^\lambda(1)}{h_l^\lambda} \int_{-1}^{1} (1-\eta^2)^{\lambda-1/2} C_l^\lambda(\eta) e^{i\pi k\eta} d\eta \right|
\end{aligned} \tag{27}$$

where C is some positive constant. The integral in the above expression has been evaluated in closed form in [5]. This result states that

$$\frac{1}{h_l^\lambda} \int_{-1}^{1} (1-\eta^2)^{\lambda-1/2} C_l^\lambda(\eta) e^{i\pi k\eta} d\eta = \begin{cases} \Gamma(\lambda) \left(\frac{2}{\pi k}\right)^\lambda i^l (l+\lambda) J_{l+\lambda}(\pi k) & k \neq 0 \\ \delta_{0l} & k = 0 \end{cases} \tag{28}$$

where $\Gamma(\cdot)$ is the gamma function and $J_v(x)$ is the v^{th}-order Bessel function of the first kind. For $k = 0$, we have

$$\left| \frac{C_l^\lambda(1)}{h_l^\lambda} \int_{-1}^{1} (1-\eta^2)^{\lambda-1/2} C_l^\lambda(\eta) e^{i\pi k\eta} d\eta \right| = C_l^\lambda(1)\delta_{0l} = \delta_{0l} \tag{29}$$

Since $|J_v(x)| \leq 1, \forall x, v > 0$, we have for $k \neq 0$

$$\begin{aligned}
\left| \frac{C_l^\lambda(1)}{h_l^\lambda} \int_{-1}^{1} (1-\eta^2)^{\lambda-1/2} C_l^\lambda(\eta) e^{i\pi k\eta} d\eta \right| &\leq C_l^\lambda(1)\Gamma(\lambda)(l+\lambda) \left(\frac{2}{\pi|k|}\right)^\lambda \\
&= \frac{\Gamma(\lambda)(l+\lambda)\Gamma(l+2\lambda)}{l!\Gamma(2\lambda)} \left(\frac{2}{\pi|k|}\right)^\lambda
\end{aligned} \tag{30}$$

where the second step is obtained for substituting for $C_l^\lambda(1)$. Summing over all k we obtain

$$\sum_{|k|\leq N} \frac{1}{d_k^3} \left| \frac{C_l^\lambda(1)}{h_l^\lambda} \int_{-1}^{1} (1-\eta^2)^{\lambda-1/2} C_l^\lambda(\eta) e^{i\pi k\eta} d\eta \right| \leq$$

$$\delta_{0l} \frac{1}{d_0^3} + \frac{\Gamma(l+2\lambda)\Gamma(\lambda)(l+\lambda)}{l!\Gamma(2\lambda)} \sum_{0<|k|\leq N} \frac{1}{d_k^3} \left(\frac{2}{\pi|k|}\right)^\lambda \tag{31}$$

Define $H(\omega_k, N, \lambda) := \sum_{0<|k|\leq N} \frac{1}{d_k^3} \left(\frac{1}{|k|}\right)^\lambda$. This term is plotted in Fig. 15 as a function of N for different values of λ. A direct comparison with the Fig. 9 (standard Fourier reconstruction) reveals the reduced impact on the error as a function of N. Eqn. 31 therefore becomes

$$\sum_{|k|\leq N} \left| \frac{C_l^\lambda(1)}{h_l^\lambda} \int_{-1}^{1} (1-\eta^2)^{\lambda-1/2} C_l^\lambda(\eta) e^{ik\pi\eta} d\eta \right|$$

$$\leq \frac{\delta_{0l}}{d_0^3} + \frac{\Gamma(l+2\lambda)\Gamma(\lambda)(l+\lambda)}{l!\Gamma(2\lambda)} \left(\frac{2}{\pi}\right)^\lambda H(\omega_k, N, \lambda) \tag{32}$$

Substituting in Eqn. 27, we obtain

$$\begin{aligned}
\|P_m S_N g - P_m S_N \tilde{g}\|_\infty &\leq C \sum_{l=0}^{m} \left(\frac{\delta_{0l}}{d_0^3} + \frac{\Gamma(l+2\lambda)\Gamma(\lambda)(l+\lambda)}{l!\Gamma(2\lambda)} \left(\frac{2}{\pi}\right)^\lambda H(\omega_k, N, \lambda) \right) \\
&= C \left(\frac{1}{d_0^3} + \frac{\Gamma(\lambda)}{\Gamma(2\lambda)} \left(\frac{2}{\pi}\right)^\lambda H(\omega_k, N, \lambda) \sum_{l=1}^{m} \frac{\Gamma(l+2\lambda)(l+\lambda)}{l!} \right) \\
&= C \left(\frac{1}{d_0^3} + H(\omega_k, N, \lambda)\rho(m, \lambda) \right), \quad \rho(m,\lambda) = \frac{\Gamma(\lambda)}{\Gamma(2\lambda)} \left(\frac{2}{\pi}\right)^\lambda \sum_{l=1}^{m} \frac{\Gamma(l+2\lambda)(l+\lambda)}{l!} \\
&\lesssim C\, H(\omega_k, N, \lambda)\, \rho(m, \lambda)
\end{aligned} \tag{33}$$

where the final step is obtained by assuming that $\frac{1}{d_0^3} \lesssim H(\omega_k, N, \lambda)\, \rho(m, \lambda)$. This is true for most problems since the low frequencies contain a significant portion of the signal energy and are therefore well sampled; i.e., $\frac{1}{d_0^3}$ is usually small.

We duly note that this bound is very conservative in the sense that $\rho(m, \lambda)$ grows rapidly with m, λ. A more focused effort on optimizing the bound will no doubt yield a more realistic value. In particular, the bound in Eqn. 30 is too conservative; the presence of the Bessel function and the imaginary term is bound to result in cancellations. However, our primary objective here is to investigate the dependence of the sampling density and number of coefficients on reconstruction accuracy. As expected, we see that the sampling density impacts the re-projection error. We also note that the error depends on N – the more gridding coefficients we use, the more error is introduced. However, unlike standard Fourier reconstruction (Eqn. 19), the error does not increase rapidly with N. The N-dependence is determined by the term $H(\omega_k, N, \lambda)$. Although $H(\omega_k, N, \lambda)$ is an increasing function in N, we observe that the rate of increase for large N is small. This indicates that the spectral re-projection procedure provides a

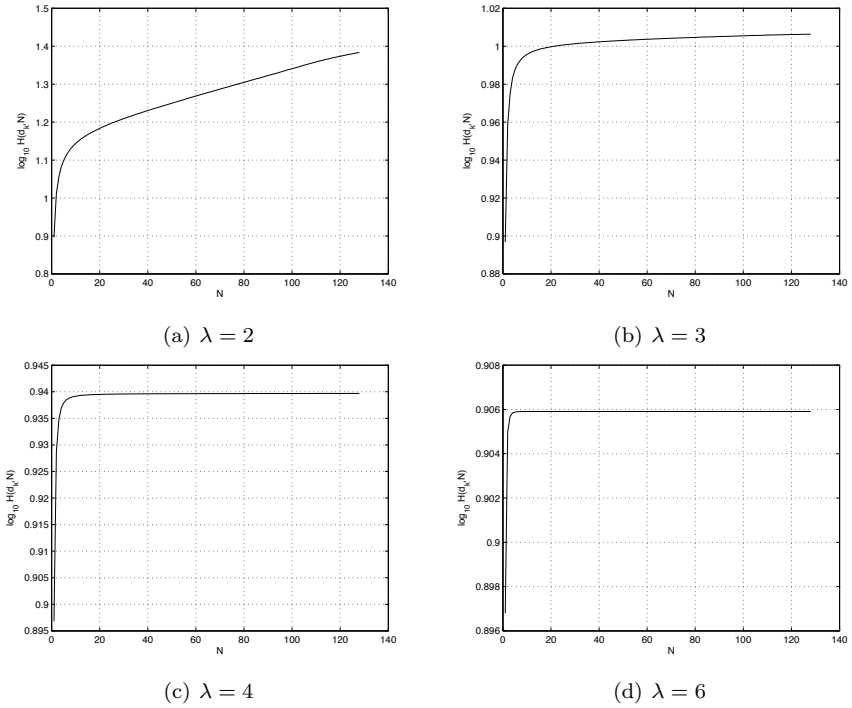

(a) $\lambda = 2$ (b) $\lambda = 3$

(c) $\lambda = 4$ (d) $\lambda = 6$

Fig. 15 Plots of $H(d_k, N, \lambda)$ as a function of N for log sampling

damping effect on the error introduced by non-uniform sampling and gridding. This trend has also been observed in simulations illustrated in Fig. 18.

The properties of the filtered Fourier and the spectral re-projection reconstructions are illustrated in the plots of Fig. 16 where test function $f_4(x)$ in Eqn. 20 is reconstructed from its log spectral samples. In either case, convolutional gridding was used to obtain the equispaced coefficients. Figs. 16(a) and (b) plot the filtered Fourier and spectral re-projection (using Gegenbauer polynomials) reconstructions respectively while Fig. 16(c) plots the log errors in the reconstructions. The Fourier reconstruction used 256 coefficients while the Gegenbauer reconstruction used just 85 coefficients. We see that equivalent error performance is obtained while avoiding Gibbs oscillations or smearing artifacts. Further numerical evidence of the effectiveness of Gegenbauer reconstruction is seen in the decay rate of the expansion coefficients. Fig. 17 plots the magnitude of the regridded Fourier coefficients alongside the Gegenbauer expansion coefficients. These coefficients correspond to the reconstruction of the test function $f_4(x)$. The Gegenbauer coefficients were computed from the 85-term Fourier expansion of $f_4(x)$. Note that the Gegenbauer expansion is computed using a five term partial sum, indicating a significantly accelerated decay rate over the standard Fourier case.

Needless to say, similar results can be obtained when using the URS algorithm to obtain equispaced coefficients. Fig. 18(a) and (b) plot the 2-norm and maximum norm errors respectively for the reconstruction of test function $f_4(x)$ (Eqn. 20) from its log spectral samples with equispaced coefficients recovered using the URS algorithm. The plots show the error as a function of N for filtered Fourier approximations (different

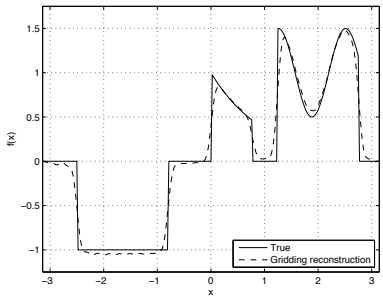

(a) Second-order exponentially filtered Fourier reconstruction, 256 coefficients

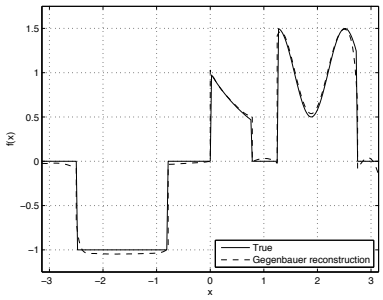

(b) Gegenbauer reconstruction, 85 coefficients

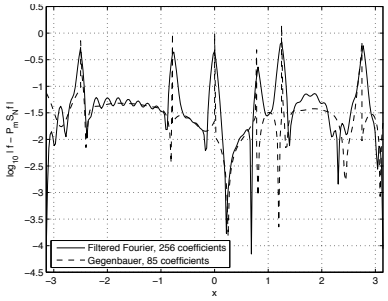

(c) Physical space log reconstruction errors

Fig. 16 Comparison of filtered Fourier and spectral re-projection reconstructions, log sampling scheme

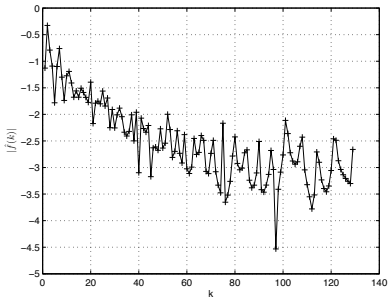

(a) Regridded Fourier coefficients

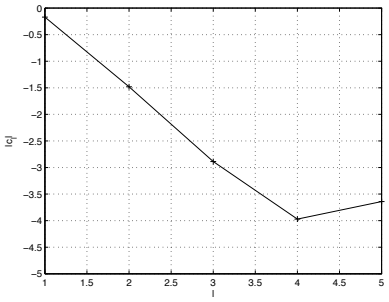

(b) Gegenbauer expansion coefficients

Fig. 17 Comparison of decay rates of Fourier and Gegenbauer expansion coefficients

order exponential filters) and the Gegenbauer reconstruction. It is important to note that, unlike the standard Fourier reconstruction (without filtering or re-projection, Fig. 10(d)), the error does not increase when we use more of the recovered equispaced coefficients. However, one notices a trend of the error curve flattening out after a certain number of coefficients. The first to flatten out and indeed the plot with the least error is the Gegenbauer curve, indicating that there are strong advantages to using spectral re-

projection methods for reconstruction from sampling schemes similar to log sampling.

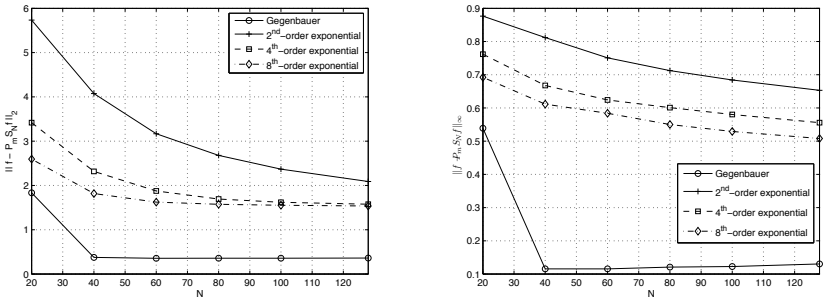

(a) 2-norm error (b) Maximum norm error

Fig. 18 Reconstruction error as a function of N (Test function $f_4(x)$ in Eqn. 20, log sampling)

In all simulations, no effort was made to optimize the parameters m and λ. These were chosen proportional to the length of the reconstruction interval with m, λ taking a minimum value of two and capped to a maximum of six and four respectively. We note that the reconstruction is more sensitive to parameter selection than re-projection with the harmonic Fourier sum. In particular, we do not know what the resolution requirements are for determining the parameters. This behavior will be investigated as part of our future work.

6 Summary and Future Directions

We have seen that Fourier approximation from non-uniformly sampled spectral data brings with it a unique set of challenges. In particular, the reconstruction error is a function of the sampling density. We summarized two reconstruction algorithms, convolutional gridding and uniform re-sampling, and derived error bounds for the former. We also looked at the application of spectral re-projection methods to the problem and found that highly accurate reconstructions can be obtained.

It is conceivable that the error bounds derived in Sec. 3 can be used in designing better gridding window functions and filters. Although straightforward, it would be a good exercise to extend the error bounds to two-dimensions and to include procedures such as oversampling, [19]. Further, we believe that it is appropriate to look at this reconstruction problem as a general ill-posed inverse problem where the use of auxiliary information (such as edge data) may be important. Preliminary experiments suggest, for example, that if we had access to jump locations and values, we can compute highly accurate function approximations. It seems natural to try and assimilate edge detection routines, such as the concentration method of edge detection, [11, 12], into this framework.

Acknowledgements This work was supported in part by National Science Foundation grants DMS 0510813 and FRG 0652833.

References

1. Ahn, C., Kim, J., Cho, Z.: High-speed spiral-scan echo planar NMR imaging. IEEE Transactions on Medical Imaging **5**(1), 2–7 (1986)
2. Archibald, R., Chen, K., Gelb, A., Renaut, R.: Improving tissue segmentation of human brain MRI through preprocessing by the Gegenbauer reconstruction method. NeuroImage **20**(1), 489–502 (2003)
3. Archibald, R., Gelb, A.: A method to reduce the Gibbs ringing artifact in MRI scans while keeping tissue boundary integrity. IEEE Transactions on Medical Imaging **21**, 305–319 (2002)
4. Atkinson, K.: An Introduction to Numerical Analysis. John Wiley & Sons (1978)
5. Bateman, H., Erdelyi, A.: Higher transcendental functions. New York (1953)
6. Cocosco, C., Kollokian, V., Kwan, R., Evans, A.: Brainweb: Online interface to a 3D MRI simulated brain database. NeuroImage **5**(4), 425 (1997)
7. Collins, D., Zijdenbos, A., Kollokian, V., Sled, J., Kabani, N., Holmes, C., Evans, A.: Design and construction of a realistic digital brain phantom. IEEE Transactions on Medical Imaging **17**(3), 463–468 (1998)
8. Dym, H., McKean, H.: Fourier series and integrals. Academic Press, New York (1972)
9. Fessler, J.A., Sutton, B.P.: Nonuniform fast Fourier transforms using min-max interpolation. IEEE Trans. Signal Process. **51**(2), 560–574 (2003)
10. Fourmont, K.: Non-equispaced fast Fourier transforms with applications to tomography. J. of Fourier Anal. and Applicat. **9**(5), 431–450 (2003)
11. Gelb, A., Tadmor, E.: Detection of edges in spectral data. Appl. Comput. Harmonic Anal. **7**, 101–135 (1999)
12. Gelb, A., Tadmor, E.: Detection of edges in spectral data II - Nonlinear Enhancement. SIAM J. Numerical Anal. **38**(4), 1389–1408 (2000)
13. Gottlieb, D., Orszag, S.: Numerical analysis of spectral methods: theory and applications. Society for Industrial and Applied Mathematics (1977)
14. Gottlieb, D., Shu, C.: On the Gibbs phenomenon and its resolution. Siam Review pp. 644–668 (1997)
15. Hesthaven, J., Gottlieb, S., Gottlieb, D.: Spectral methods for time-dependent problems. Cambridge University Press (2007)
16. Jackson, J.I., Meyer, C.H., Nishimura, D.G., Macovski, A.: Selection of a convolution function for Fourier inversion using gridding. IEEE Trans. Med. Imag. **10**(3), 473–478 (1991)
17. Kwan, R., Evans, A., Pike, G.: MRI simulation-based evaluation of image-processing and-classification methods. IEEE Transactions on Medical Imaging **18**(11), 1085–1097 (1999)
18. McConnell Brain Imaging Center: BrainWeb: Simulated Brain Database. http://www.bic.mni.mcgill.ca/brainweb/
19. O'Sullivan, J.D.: Fast sinc function gridding algorithm for Fourier inversion in computer tomography. IEEE Trans. Med. Imag. **4**(4) (1985)
20. Pipe, J.G., Menon, P.: Sampling density compensation in MRI: Rationale and an iterative numerical solution. Magnetic Resonance in Medicine **41**(1), 179–186 (1999)
21. Remi, K., Evans, A., Pike, G.: An extensible MRI simulator for post-processing evaluation. In: Proceedings of the 4th International Conference on Visualization in Biomedical Computing, pp. 135–140. Springer (1996)
22. Rosenfeld, D.: An optimal and efficient new gridding algorithm using singular value decomposition. Magnetic Resonance in Medicine **40**(1), 14–23 (1998)
23. Rosenfeld, D.: New approach to gridding using regularization and estimation theory. Magnetic Resonance in Medicine **48**(1), 193–202 (2002)
24. Steidl, G.: A note on fast Fourier transforms for nonequispaced grids. Advances in Computational Math. **9**(3), 337–352 (1998)
25. Tadmor, E.: Filters, mollifiers and the computation of the Gibbs phenomenon. Acta Numerica **16**, 305–378 (2007)

26. Tadmor, E., Tanner, J.: Adaptive mollifiers for high resolution recovery of piecewise smooth data from its spectral information. Foundations of Computational Mathematics **2**(2), 155–189 (2002)
27. Tadmor, E., Tanner, J.: Adaptive filters for piecewise smooth spectral data. IMA Journal of Numerical Analysis **25**(4), 635–647 (2005)
28. Tadmor, E., Zou, J.: Three Novel Edge Detection Methods for Incomplete and Noisy Spectral Data. Journal of Fourier Analysis and Applications **14**(5), 744–763 (2008)